Stereodynamics of the Reaction $O(^1D_2) + H_2(v=0) \rightarrow OH(X^2\Pi_i; v'=0, N', f) + H$: State-Resolved Linear and Rotational Angular Momentum Distributions

A. J. Alexander,[†] F. J. Aoiz,[‡] L. Bañares,[‡] M. Brouard,[†] J. Short,[†] and J. P. Simons*[,†]

Physical and Theoretical Chemistry Laboratory, South Parks Road, Oxford, OX1 3QZ, UK, and Departamento de Química Física, Facultad de Química, Universidad Complutense, E-28040 Madrid, Spain

Received: March 31, 1997; In Final Form: May 30, 1997[⊗]

The product-state-specific stereodynamics of the photon-initiated reaction of $O(^1D_2)$ with H_2 has been investigated by polarized Doppler-resolved laser-induced fluorescence, under room-temperature bulb conditions. Product-state-resolved differential cross sections, excitation functions, and rotational angular momentum alignments are reported for the channels leading to $OH(^2\Pi_{3/2}(A'/A''); v'=0, N'=5)$ and $OH(^2\Pi_{1/2}(A'); v'=0, N'=14)$ at a mean collision energy of ~12 kJ mol^{-1}. The data are compared with (state-resolved) quasi-classical trajectory (QCT) calculations of the linear and angular momentum distributions and excitation functions conducted on the Schinke−Lester (SL1) ab initio ground-state potential energy surface, under similar conditions as the experiments. Overall, excellent agreement is obtained between the QCT calculated and experimentally determined stereodynamical features. The results are discussed in light of other recent work on this prototypical insertion reaction and on the related systems $O(^1D_2) + HD$ and CH_4.

I. Introduction

Polarized Doppler-resolved laser spectroscopy has expanded the laser "pump−probe" technique from the scalar to the vectorial arena to provide a key general method that is sensitive to both the linear and rotational angular momentum distributions among the scattered products of reactive (or inelastic) collisions. The technique is, necessarily, state-selective since it involves optical detection (e.g., laser-induced fluorescence (LIF) or ionization (REMPI)), allowing vectorial distributions to be determined for individually populated quantum states,[1,2] and their direct comparison with those computed through quasi-classical trajectory (QCT) or quantum scattering calculations on ab initio or trial potential energy surfaces. In classical terms, the swarm of reactive trajectories can be resolved into subsets, populating individual channels, and checked against experimental observation to provide an extraordinarily detailed, "laboratory-tested", dynamical picture of the course of individual reactive collisions.

The strategy has been particularly effective in probing the stereodynamics of photon-initiated bimolecular reactions through the sequence

$$AD + h\nu(\text{pol}) \rightarrow A_t + D$$

$$A_t + BC \rightarrow AB(v',j') + C$$

Velocity-aligned atomic (or molecular) reagents are generated through the polarized photodissociation of an appropriate source, and the molecular products scattered from their subsequent collision (in either a bulb[3] or a molecular beam environment[4]) are probed, after a short delay, by the polarized, probe laser. If the rotational angular momentum of the scattered product, AB-(v',j'), were unpolarized, its Doppler-resolved spectrum would simply reflect its speed distribution along the detection axis. When C is a structureless atom, transformation from the laboratory (LAB) to the center−of−mass (CM) frame provides the product-state-resolved differential cross section (DCS) directly,[5,6] i.e., the vector correlation between the reagent **k** and product **k′** relative velocities.

In general, the rotational angular momentum distribution of $AB(v',j')$ *will* be polarized, and the Doppler-resolved spectrum will be sensitive to the correlations between **k**,**k′** and **j′**, the product rotational angular momentum. Their full spatial distribution in the CM frame, $P(\mathbf{k},\mathbf{k}',\mathbf{j}')$, can be expressed in terms of a set of generalized, polarization−dependent differential cross sections (PDDCS),[7] which are, in effect, scattering-angle-dependent multipole moments of $P(\mathbf{k},\mathbf{k}',\mathbf{j}')$. They can be related to the bipolar moments of the LAB frame distribution determined from the experimental Doppler contours[8] to provide the (low-order) moments of the $P(\mathbf{k},\mathbf{k}',\mathbf{j}')$ distribution and thereby the azimuthally averaged correlations $(\mathbf{k},\mathbf{k}')$, $(\mathbf{k},\mathbf{j}')$, and $(\mathbf{k}',\mathbf{j}')$, together with the triple vector correlation, $(\mathbf{k},\mathbf{k}',\mathbf{j}')$. Since the triple correlation depends upon the dihedral angle between the scattering plane, **k**,**k′**, and the **k**,**j′** plane, its determination reveals dynamical features that are normally obscured by the azimuthal averaging associated with the random distribution of collision impact parameters.[9]

The ability to determine these correlations for individually resolved quantum states and to compare the measurements with those predicted by QCT[8,10] or quantum scattering calculations[11] has opened a new era in the field of molecular reaction dynamics. The present paper describes the current status of a long-term, experimental and computational study of the stereodynamics of the benchmark reaction

$$O(^1D_2) + H_2 \rightarrow OH(X^2\Pi_i; v', N', f) + H \qquad (1)$$

and explores the dynamical similarities with the "sister" reaction of $O(^1D_2)$ with CH_4. A preliminary account of some of the work has appeared elsewhere.[12] Section II provides an outline of the experimental and analytical procedures; section III summarizes the experimental and computational (QCT) results; section IV discusses their interpretation and their relationship to recent studies of the reaction with CH_4;[13,14] section V offers a "forward look".

* Corresponding author.
[†] Physical and Theoretical Chemistry Laboratory.
[‡] Universidad Complutense.
[⊗] Abstract published in *Advance ACS Abstracts,* September 15, 1997.

S1089-5639(97)01123-7 CCC: $14.00

II. Methods

A. Experimental Procedures. These have been amply documented elsewhere[12,13] so only a brief summary will be given here. $O(^1D_2)$ atomic reagents, generated via photodissociation of N_2O using linearly polarized ArF laser radiation at 193 nm, were allowed to collide with H_2 under "bulb" conditions at room temperature. The OH radicals, scattered through reaction under single-collision conditions, were detected by a second polarized laser, delayed by 200 ns ($N' = 5$ data) or 110 ns ($N' = 14$ data) and tuned to excite transitions in the OH(A←X) laser-induced fluorescence (LIF) spectrum. The total pressure in the flowing 1:1 gas mixture was held at 13.3 Pa ($N' = 5$ data) or 11.0 Pa ($N' = 14$ data). Doppler-resolved LIF spectra of OH were recorded using three alternative excitation-detection geometries (cases A, B, and D[15,16]). For $N' = 5$ the $^2\Pi_{3/2}$ state was probed with the main R_{11} and Q_{11} and satellite P_{21} and Q_{21} transitions, and for $N' = 14$ the $^2\Pi_{1/2}$ state was probed with the main P_{22} and the satellite Q_{12} transitions. This enabled the two lambda-doublet components, $\Pi(A')$ and $\Pi(A'')$, to be probed separately for each level. The probe laser bandwidth was measured to be 0.10 ± 0.01 cm^{-1}. Spectral saturation was avoided by frequent measurements of the relative intensities of the main and satellite lines or by ensuring a linear relationship between the probe power and the integrated intensity. The absence of collisional relaxation was established by checking the insensitivity of the Doppler contours to changes in the probe laser delay time. Successive spectra were summed to achieve adequate signal−to−noise ratios. The normalization procedures followed those employed in earlier studies.[13,17]

B. Analytical Procedures. *1. Doppler Profiles.* Composite Doppler profiles, constructed by summing appropriate sets of experimental data recorded using alternative geometries and rotational transitions,[13,17] were used to project out individual moments of the vectorial distribution $P(\mathbf{k},\mathbf{k}',\mathbf{j}')$. The corresponding Doppler line shape functions may be written as[8,17]

$$D_0^K(k_1,k_2;v_p) = \int_{v=v_p}^{\infty} (1/2v)\, \overline{\beta_0^K}(k_1,k_2;v)\, P_{k_1}(v_p/v)\, dv \quad (2)$$

where v is the speed of the product and v_p is the component of $\mathbf{v}$ along the probe laser propagation axis. The $\overline{\beta_0^K}(k_1,k_2;v)$ coefficients are the rescaled laboratory frame bipolar moments[8] averaged over the spread of atomic and molecular reagent velocities, and P_{k_1} are Legendre polynomials. In the present context, the composite profiles of prime concern are (i) $D_0^0(0,0;v_p)$, which reflects the laboratory speed distribution of the scattered products (and for a triatomic system at fixed collision energy, the CM DCS, $\mathbf{k}$, $\mathbf{k}'$), (ii) $D_0^2(2,0;v_p)$, which reflects the product angular distribution in the laboratory frame, and (iii) the set $D_0^2(0,2;v_p)$, $D_0^0(2,2;v_p)$, and $D_0^2(2,2;v_p)$, which reflects the product rotational polarization, again in the laboratory frame.

The full spatial distribution of the three vectors, $\mathbf{k}$, $\mathbf{k}'$, and $\mathbf{j}'$, in the CM frame, can be expressed as an expansion in modified spherical harmonics.[7,8] The moments of the distribution (the expansion coefficients) can be written either as a set of bipolar moments or a set of generalized polarization-dependent differential cross sections (PDDCSs), $(1/\sigma)(d\sigma_{kq}/d\omega_t)$, i.e.

$$P(\omega_t,\omega_r) = \sum_k \sum_q \frac{2k+1}{4\pi} \frac{1}{\sigma} \frac{d\sigma_{kq}}{d\omega_t} C_{kq}(\omega_r)^* \quad (3)$$

where $\omega_t \equiv (\theta_t,\phi_t{=}0)$ and $\omega_r \equiv (\theta_r,\phi_r)$ represent the polar coordinates of the product velocity, $\mathbf{k}'$, and the product angular momentum, $\mathbf{j}'$, referenced to the $\mathbf{k}-\mathbf{k}'$ scattering plane. The $C_{kq}(\theta_r,\phi_r)$ are the modified spherical harmonics. The moments of the distribution can be related to the laboratory frame moments determined from the Doppler contours by expressing the experimental contours as expansions in sets of contracted basis functions, $G_0^K(k_1,k_2;v_p;k',q)$, averaged over the full three-dimensional spread of reagent velocities[8,17]

$$D_0^K(k_1,k_2;v_p) = \sum_{k'} \sum_{q\geq 0} m_{k_2 q\pm}^{k'} G_0^K(k_1,k_2;v_p;k',q) \quad (4)$$

and following a least-squares fitting procedure. Analysis of the profiles identified in (i) and (ii) above, which have $K = k_1 = 0$ or 2, $k_2 = k = 0$, and $q = 0$, yields the Legendre moments of the (conventional) differential cross section,

$$\frac{2\pi}{\sigma}\frac{d\sigma}{d\omega_t} \equiv \frac{1}{\sigma}\frac{d\sigma_{00}}{d\cos\theta_t} = \frac{1}{2}\sum_{k'} m_{00}^{k'} P_{k'}(\cos\theta_t) \quad (5)$$

Because of the spread of $O(^1D)$ velocities (see below), and hence reaction collision energies, E_t, it was found necessary to allow for the effects of an excitation function, i.e., collision energy dependence of the reaction cross section, $\sigma(E_t)$, in the data fitting. This is included as a separate expansion in Legendre−contracted basis functions in reagent translational energy, which are fitted simultaneously with the DCS. Random sampling ensures that the full range of parameters (e.g., $\cos\theta_t$ or E_t) are included in the simulations of the Legendre moment contracted basis sets. The resolution is determined by the truncation point of the series in eq 4. In the fitting of the profiles $D_0^0(0,0;v_p)$ and $D_0^2(2,0;v_p)$, for example, five moments were required in E_t and up to six moments were employed in $\cos\theta_t$. The method of fitting, however, assumed no dependence of the DCS on E_t.

The remaining PDDCSs with $k = 2$ and $q = 0$, 1 and 2,[8,17] namely $(1/\sigma)(d\sigma_{20}/d\omega_t)$, $(1/\sigma)(d\sigma_{21-}/d\omega_t)$, and $(1/\sigma)(d\sigma_{22+}/d\omega_t)$, which reflect (even moments of) the full angular momentum distribution, $P(\mathbf{k},\mathbf{k}',\mathbf{j}')$, were extracted using a procedure analogous to the DCS. Each bipolar moment is dependent on the three PDDCSs, and simultaneous fits to the three composite profiles listed in (iii) using eq 4 yield the expansion moments of each renormalized PDDCS written in the form[8,17]

$$\left(\frac{1}{\sigma}\frac{d\sigma_{kq\pm}}{d\omega_t}\right) \Big/ \left(\frac{1}{\sigma}\frac{d\sigma_{00}}{d\omega_t}\right) = \sum_{k'} m_{kq\pm}^{k'} C_{k'+q}(\theta_t, 0) \quad (6)$$

Least-squares minimization was employed to extract two expansion coefficients for each renormalized PDDCS, with the latter constrained to the limiting values identified previously by Aoiz et al.[8] Integration of the PDDCSs over some or all of the scattering angles, θ_t, provides rotational angular momentum distributions $P(\mathbf{k},\mathbf{j}')$ and polarization parameters, $a_{q\pm}^k$[7,8] (see section IIB3), averaged over some or all of the scattering angular distribution. (Note: although odd moments of the full distribution cannot be determined in the present experiments, which use linearly polarized light, they may be accessed in the future by employing a circularly polarized probe laser; they may also be extracted from the results of QCT calculations, which necessarily provide the full angular momentum distribution;[10] see below.)

2. $O(^1D_2)$ Source. In analyzing the experimental data, account has been taken of two new photofragment imaging studies of the photodissociation dynamics of N_2O at wavelengths in the region of 200 nm.[18,19] These indicate a strong dependence of the translational anisotropy, $\beta(O(^1D_2))$, on the atomic recoil speed. At low speeds, in particular, the anisotropy falls well below the average value, $\bar{\beta} \approx 0.48$, determined through time-of-flight measurements[20] and averaged over the full speed distribution. In addition, there is clear evidence of an orbitally

aligned distribution in the $O(^1D_2)$ population, which greatly complicates the determination of the true translational anisotropy, $\beta(v(O(^1D_2))$. Because of this, the DCSs for $OH(v'=0,N'=5$ and 14) were initially determined by restricting the analysis to the (isotropic) laboratory speed-dependent contour, $D_0^0(0,0;v_p)$, which is independent of $\beta(O(^1D_2))$ and relatively insensitive to the excitation function, $\sigma(E_t)$. When the contour reflecting the products' angular distribution, $D_0^2(2,0;v_p)$, was also included in the analysis, however, the profile could only be successfully reproduced when the DCS was complemented by an excitation function, $\sigma(E_t)$, heavily weighted in favor of low collision energies, coupled with a "best-fit" value of $\bar{\beta} \simeq 0.2-0.3$ over the effective collision energy range—a result in good agreement with expectations based upon photofragment imaging studies. The excitation function and the value of $\bar{\beta}$ were similarly employed in the analysis of the rotational angular momentum polarization. Although the above procedure provides a self-consistent analysis of the rotational polarization and cross-section data, the excitation functions extracted from the experiments are highly sensitive to the assumed form of the $O(^1D)$ speed distribution and the translational anisotropy, $\beta(v(O(^1D_2))$, both of which remain to be determined with high precision in the critical, low $O(^1D)$ speed region. We emphasize that, in contrast, the returned DCSs and PDDCSs are little affected by the assumed form of the $O(^1D)$ velocity distribution, provided both analyses employ the "best-fit" value of $\bar{\beta}$ described above.

3. Quasi-Classical Trajectory Calculations. The QCT method used is similar to the one described in previous publications (see, for instance, ref 21), and only the details relevant to the present work will be given here. All the calculations were performed on a slightly modified version of the Schinke−Lester SL1 potential energy surface (PES)[22] as indicated in ref 23 (referred to as SL1MS PES). This PES yields very similar results to the original SL1, although some changes in the total cross section can be observed below 0.1 eV.

A batch of 600 000 trajectories was run for the $O(^1D) + H_2(v=0,j=1)$ reaction at a fixed collision energy of 0.1 eV (9.65 kJ mol^{-1}). The experimental mean collision energy is 0.12 eV (11.6 kJ mol^{-1}) with a standard deviation of 0.07 eV (6.8 kJ mol^{-1}), which corresponds to a fwhm of 0.16 eV (15.5 kJ mol^{-1}). Thus, calculations at 0.1 eV and initial $j = 1$ roughly correspond to the mean collision energy and the most populated H_2 rotational level (300 K) of the present experiment. Rovibrational quantization was introduced by fitting the asymptotic limits of the potential using the semiclassical action integral. The resultant rovibrational energies were fitted to a Dunham expansion. The assignment of product quantum numbers v',j' is carried out by equating the classical rotational angular momentum of the OH molecule to $[j'(j'+1)]^{1/2}\hbar$. (We reserve the j and j' notation for the nuclear rotational angular momentum quantum numbers employed in the QCT calculations.) With the (real) j' value so obtained, the vibrational quantum number v' is found by equating the internal energy of the OH molecule to the corresponding Dunham expansion. The values of v' and j' found in this way are then rounded to the nearest integer. The integration time step was 2×10^{-17} s. This guarantees conservation of the total energy to better than 1 in 10^5 and better than 1 in 10^7 in the total angular momentum.

The trajectory results were used to obtain vector correlations for the OH product born in individual rovibrational states $v' = 0, j' = 5$ and $v' = 0, j' = 14$. In the semiclassical approximation, the PDDCSs of Shafer et al.[7] can be expressed as series of modified spherical harmonics,[8]

$$\frac{1}{\sigma}\frac{d\sigma_{kq\pm}}{d\omega_t} = \sum_{k_1}\frac{[k_1]}{4\pi}s_{kq\pm}^{k_1}C_{k_1-q}(\theta_t, 0) \qquad (7)$$

where $[k] \equiv 2k + 1$. (This equation may be compared with eq 6, which is an analogous expansion but for the renormalized PDDCSs.) The coefficients of the expansion, $s_{kq\pm}^{k_1}$, are calculated as

$$s_{kq\pm}^{k_1} = (-1)^q\, 2i\langle C_{k_1q}(\theta_t, 0)\, C_{kq}(\theta_r, 0) \sin q\phi_r\rangle \qquad k \text{ odd}$$

$$= (-1)^q\, 2\langle C_{k_1q}(\theta_t, 0)\, C_{kq}(\theta_r, 0) \cos q\phi_r\rangle \qquad k \text{ even} \quad (8)$$

where the brackets indicate the averaging over all the trajectories leading to a given rovibrational state. The symmetry constraints resulting from the invariance of the distribution of product OH internuclear axis requires

$$s_{kq+}^{k_1} = 0 \qquad k, q \text{ different parity}$$

$$s_{kq-}^{k_1} = 0 \qquad k, q \text{ same parity}$$

The joint probability density function of the angles θ_r and ϕ_r, which define the direction of $\mathbf{j}'$, can be obtained by integrating the full $\mathbf{k}$, $\mathbf{k}'$, $\mathbf{j}'$ distribution, given by eq 3, over scattering angle to give the expression

$$P(\theta_r, \phi_r) = \frac{1}{4\pi}\sum_{kq}[k]a_q^k C_{kq}(\theta_r, \phi_r)^*$$

$$= \frac{1}{4\pi}\sum_k\sum_{q\geq 0}[k][a_{q\pm}^k \cos q\phi_r - a_{q-}^k\, i \sin q\phi_r]C_{kq}(\theta_r, 0) \quad (9)$$

where the upper sign in the second line of eq 9 is associated with even q and the lower sign with odd q. The maximum value of k in the summation is $2j'$, although fewer terms are normally sufficient to get a good convergence. The polarization parameters, a_q^k, are defined as

$$a_q^k = 2\pi\int_{-1}^{1}\frac{1}{\sigma}\frac{d\sigma_{kq}}{d\omega_t}d(\cos\theta_t), \quad a_{q\pm}^k = a_q^k \pm a_{-q}^k \qquad (10)$$

for which the symmetry constraints imply

$$a_{q+}^k = 0 \qquad (k \text{ even}, q \text{ odd}) \quad \text{or} \quad (k \text{ odd}, q \text{ even})$$

$$a_{q-}^k = 0 \qquad (k \text{ even}, q \text{ even}) \quad \text{or} \quad (k \text{ odd}, q \text{ odd})$$

$$a_0^k = 0 \qquad \text{for } k \text{ odd}$$

In the QCT calculations, the polarization parameters are evaluated as

$$a_{q\pm}^k = 2\langle C_{k_1|q|}(\theta_r, 0) \cos q\phi_r\rangle \qquad k \text{ even}$$

$$a_{q\pm}^k = 2i\langle C_{k_1|q|}(\theta_r, 0) \sin q\phi_r\rangle \qquad k \text{ odd} \qquad (11)$$

which, for $q = 0$, reduces to $a_0^k = \langle P_k(\cos\theta_r)\rangle$. As above, the brackets indicate the averaging over the whole set of trajectories leading to a chosen rovibrational state. In terms of expectation values, the first polarization parameters are

$$a_{1+}^1 = -i\sqrt{2}\langle \sin\theta_r \sin\phi_r\rangle = -i\sqrt{2}\langle j_y'/j'\rangle$$

$$a_0^2 = \langle P_2(\cos\theta_r)\rangle = \langle (3j_z'^2 - j'^2)/2j'^2\rangle$$

$$a_{1-}^2 = -\sqrt{6}\langle \sin\theta_r \cos\theta_r \cos\phi_r\rangle = -\sqrt{6}\langle j_x' j_z'/j'^2\rangle$$

$$a_{2+}^2 = \sqrt{3/2}\langle \sin^2\theta_r \cos 2\phi_r\rangle = \sqrt{3/2}\langle (j_x'^2 - j_y'^2)/j'^2\rangle$$

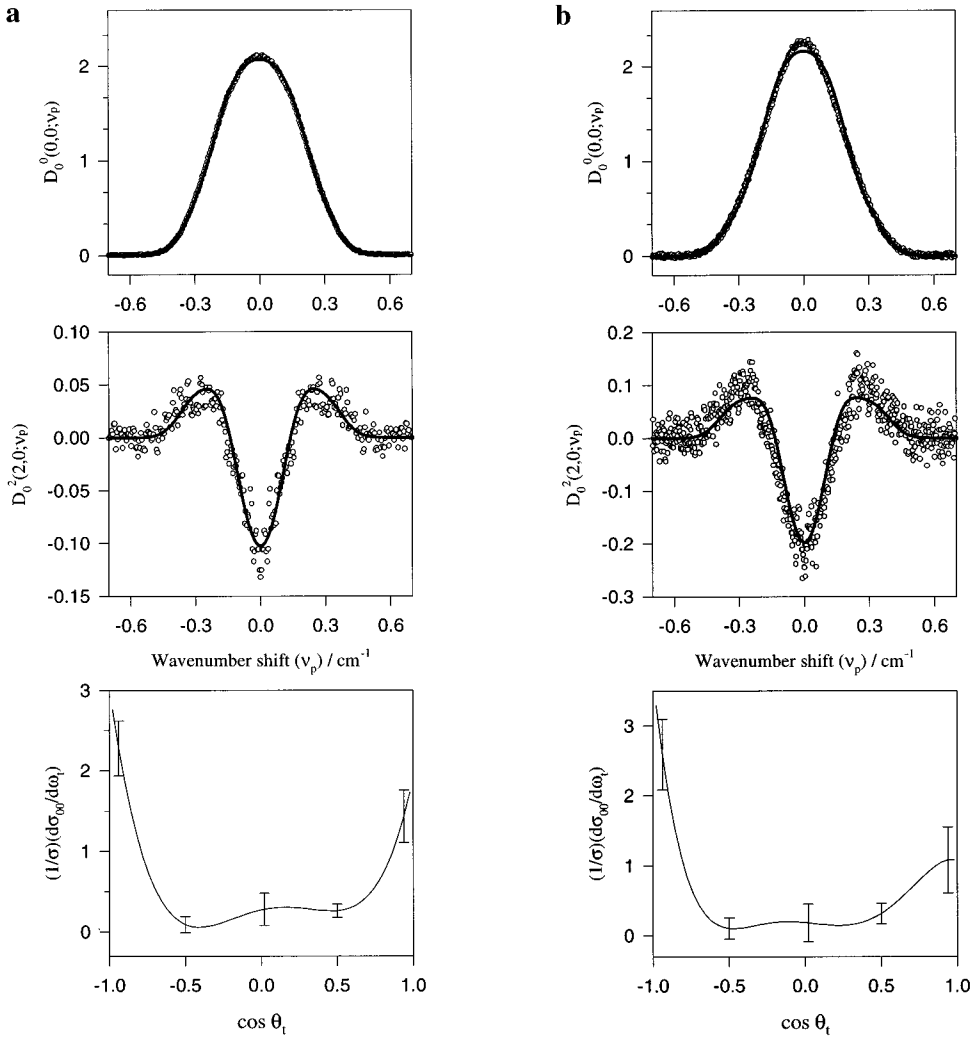

Figure 1. (a) Experimental composite profiles $D_0^0(0,0;v_p)$ (top panels) and $D_0^2(2,0;v_p)$ (middle panels), which depend on the LAB speed and LAB translational anisotropy, for (a) OH(v'=0,N'=14,A′) and (b) OH(v'=0,N'=5), averaged over the A′ and A″ lambda-doublet levels. The experimental data are shown as points, and the solid lines are fitted Doppler contours corresponding to the derived DCSs and $\sigma(E_t)$ (see Figure 2). The DCSs in the lower panels are shown as moment expansions in Legendre polynomials, as discussed in the text. The sampled error bars are single σ uncertainties.

where j'_x, j'_y, and j'_z are the components of $\mathbf{j}'$ along the *x*, *y*, and *z* axes, respectively. Therefore, the polarization parameters are just the expectation values of the multipole moments of the expansion of *j*. Notice that $a_0^1 \propto \langle j'_z/j' \rangle$ and $a_{1-}^1 \propto \langle j'_x/j' \rangle$ are null for nonchiral systems; the system can be *aligned but not oriented* along the *x* and *z* axes. The distribution of θ_r and ϕ_r may be presented as a three-dimensional polar plot, as illustrated in sections IIIB and IVC.

As commented on above, the analysis of the Doppler profiles required the state-specific excitation function to be taken into account, i.e., the collision energy dependence of the reaction cross section, $\sigma(E_t)$, for the individual v',j' state probed. The QCT energy-dependent reaction cross sections were calculated using a methodology similar to that presented in previous work.[24,25] In addition to the usual set of initial conditions, the collision energy, E_t, and the initial rotational quantum number of the reactants, *j*, were each randomly sampled for every trajectory; E_t was uniformly sampled between $E_1 = 0.005$ eV and $E_2 = 0.5$ eV, while *j* was sampled according to the Boltzmann distribution at the temperature of the experiment, 300 K.

The maximum impact parameter for this reaction decreases rapidly with E_t, and it was necessary to adopt a procedure to select the maximum impact parameter at each collision energy. The impact parameter for each trajectory was obtained by randomly sampling between zero and a maximum value, $b_{max}(E_t, j)$, given by the expression

$$b_{max}(E_t, j) = D(1 + E_D/E_t)^{1/2} \qquad (12)$$

where *D* and E_D were obtained previously, by fitting the values of the maximum impact parameters (found by running small batches of trajectories at several selected collision energies and initial *j*) to the functionality of eq 12. The parameters *D* and E_D were chosen to lie well above the range of reactive trajectories occurring at the given collision energy and rotational state, *j*. (In practice, the same pair of *D* and E_D values could be employed for all initial *j*.) With this kind of energy-dependent sampling of the maximum impact parameter, each trajectory was weighted by $w_i = b_{max}^2/D^2$.

A batch of 10^6 trajectories was run employing the above initial conditions in order to obtain good statistics for the reactive channels producing OH(v'=0,j'=5,14). As in previous work,[24,25] the excitation function, $\sigma(E_t)$, was subsequently extracted from the trajectory data by the method of moments expansion in Legendre polynomials. This batch of trajectories was also used to obtain the collision energy dependence of the $v' = 0$, $j' = 5$, and $j' = 14$, state-resolved DCSs, averaged over initial *j* according to the Boltzmann distribution at 300 K. Full details of the methodology and the relevant equations will be presented in a forthcoming publication.[26] Suffice it to say here that the procedure consists of a bidimensional (scattering angle collision

energy) fit to a double series of Legendre polynomials with variables cos θ_t and $x = (2E_t - E_2 - E_1)/(E_2 - E_1)$, where E_1 and E_2 define the boundaries of the collision energy for which trajectories were calculated. From this double series, DCSs at a given collision energy within the interval $[E_1,E_2]$ could be calculated, which agree, within the statistical uncertainty, with those obtained from trajectories calculated at a fixed collision energy. Integration of this double series generates the series representing the excitation function. This method is ideally suited for the simulation of experiments where there is a spread of collision energies as in the present case: convolution of the energy-dependent DCS with the experimental energy distribution yields an "average" DCS, directly comparable with the one derived experimentally.

III. Results

A. State-Resolved Differential Cross Sections and Excitation Functions. The "LAB speed-dependent" and the "angular-dependent" Doppler profiles, $D_0^0(0,0;v_p)$ and $D_0^2(2,0;v_p)$ determined for the $\Pi(A')$ lambda doublet of $OH(^2\Pi_{1/2};v'=0,N'=14)$ are shown in Figure 1a. Virtually identical profiles were also recorded for the $\Pi(A'')$ lambda-doublet state, which parallels the result reported earlier for $OH(^2\Pi_{3/2};v'=0,N'=5)$;[12] the corresponding data are reproduced in Figure 1b, but this time summed over both the $\Pi(A')$ and $\Pi(A'')$ states to enhance the signal−to−noise ratio. The state-resolved DCSs, obtained from the "speed−dependent" contours via the analytical procedures outlined in section IIB1, are shown in the lower panels of Figure 1. The quality of the fit can be gauged by comparing the overlap of the experimental and analytical Doppler contours. Improved fits may be obtained by including higher Legendre moments in the $\sigma(E_T)$ distribution or by using a nonseparable fitting procedure which allows for a translational energy-dependent DCS. The (average) DCS does not change significantly between these methods, however.

The analytical contours superimposed on the experimental "angular-dependent" profiles, $D_0^2(2,0;v_p)$, were computed using the derived DCSs and excitation functions, but allowing the average reagent anisotropy, $\bar{\beta}(O(^1D_2))$, to float. The optimized excitation functions, shown in Figure 2, can be modeled by the expression $\sigma(E_t) \propto E_t^{-n}$ with n between 0.55 ($N' = 14$) and 1.1 ($N' = 5$), consistent with an absence of any barrier in the entrance channel. The optimized translation anisotropy of the reacting $O(^1D_2)$ was between 0.2 and 0.3, as noted above.

The comparison between the theoretical and the experimentally deduced state resolved excitation functions is displayed in Figure 2. The general shape of the experimental $\sigma(E_t)$ is reproduced by the calculations. However, the energy dependence of the reaction cross section used in the fit of the experimental composite Doppler profiles is clearly sharper than the theoretical one in both cases. To the best of our knowledge there are no QM state-resolved calculations of $\sigma(E_t)$; however, the agreement between the QM *total* cross section, calculated using time-dependent methods,[32] and the corresponding QCT result is excellent. As noted in section IIB2, the most likely source of the disagreement between the QCT and experimental excitation functions is the uncertainty in the $O(^1D_2)$ velocity distribution, at low velocities.

Figures 3 and 4 show the QCT calculated energy-dependent DCSs for the production of $OH(v'=0,j'=5)$ and $OH(v'=0,j'=14)$, respectively, in the collision energy range 0.01−0.40 eV. As can be seen, in both cases the DCS does not change very much with collision energy. In general, there is a predominance of backward scattering, especially for $j' = 14$. At the lowest energies (below 0.05 eV), backward scattering becomes much larger than forward scattering.

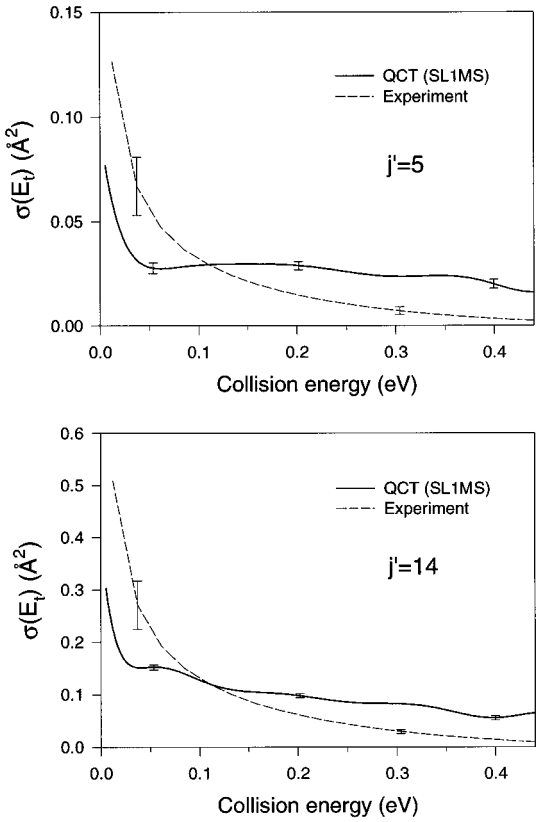

Figure 2. Excitation functions for the production of $OH(v'=0,j'=5)$ (top) and $OH(v'=0,j'=14)$ (bottom). Solid line: QCT results averaged on initial rotational H_2 states at 300 K. The error bars represent one standard deviation. This calculation has been carried out by uniform sampling of the collision energy in the range 0.005−0.5 eV. The dashed lines correspond to the optimized experimental excitation functions and their single σ uncertainties.

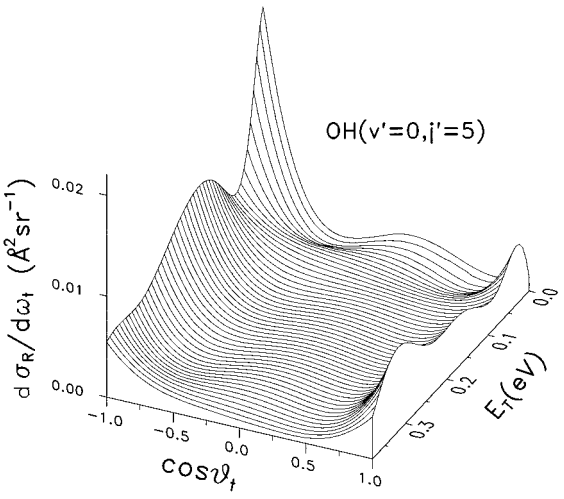

Figure 3. QCT collision energy dependence of the differential cross section for the $OH(v'=0,j'=5)$ products calculated on the SL1MS PES. The range of collision energies is 0.02−0.40 eV.

The calculated state−resolved DCSs for $j' = 5$ and $j' = 14$ are shown in Figure 5. The solid lines in the figure represent the average DCSs obtained by convoluting the energy-dependent DCSs (shown in Figures 3 and 4) with the experimental collision energy distribution. For comparison purposes, the results obtained from the QCT calculations at fixed, 0.1 eV collision energy and initial $j = 1$ are also shown as dashed lines. Both sets of calculations yield essentially the same DCSs. The agreement between the experimentally derived DCSs and those determined from the QCT calculations is good (see Figure 6),

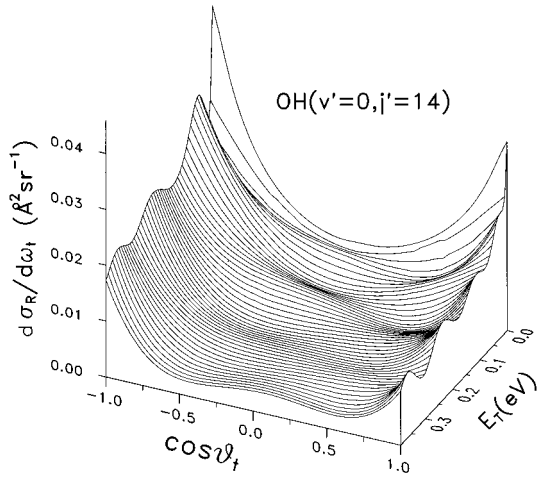

Figure 4. As in Figure 3, but for the OH(v'=0,j'=14) products. In this case, the range of collision energies is 0.01−0.40 eV.

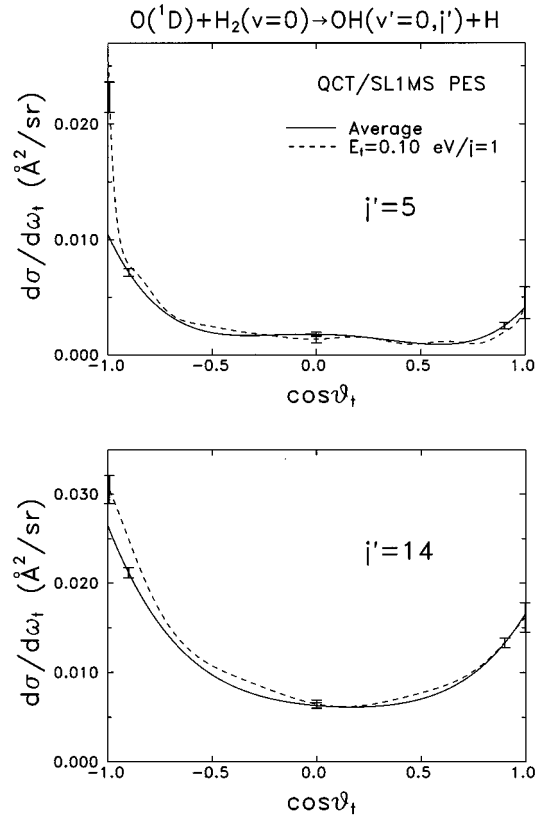

Figure 5. Differential cross sections obtained by QCT calculations for the production of OH(v'=0,j'=5) (top) and OH(v'=0,j'=14) (bottom). The solid line is the DCS averaged over the experimental collision energy distribution, $P(E_t)$, and initial j at 300 K, obtained by convoluting the data shown in Figures 2 and 3 with the experimental $P(E_t)$. For comparison purposes, the DCS obtained from the QCT calculations at $E_t = 0.1$ eV and initial $j = 1$ are shown as dashed lines. The error bars represent one standard deviation.

although for $j' = 14$, the experiment seems to yield somewhat sharper forward and backward scattering than predicted in the calculations.

B. Rotational Polarization. Composite Doppler profiles, $D_0^2(0,2;v_p)$, $D_0^0(2,2;v_p)$, and $D_0^2(2,2;v_p)$, sensitive to the laboratory (LAB) frame rotational alignment of OH in the Π(A′) and Π(A″) lambda-doublet levels of $v' = 0$, $N' = 5$ and in the Π-(A′) level of $N' = 14$, together with the fits to the data obtained following the procedures described in section IIB1, are shown in Figures 7 and 8. The derived PDDCSs, which reflect the variation in CM rotational polarization with scattering angle,

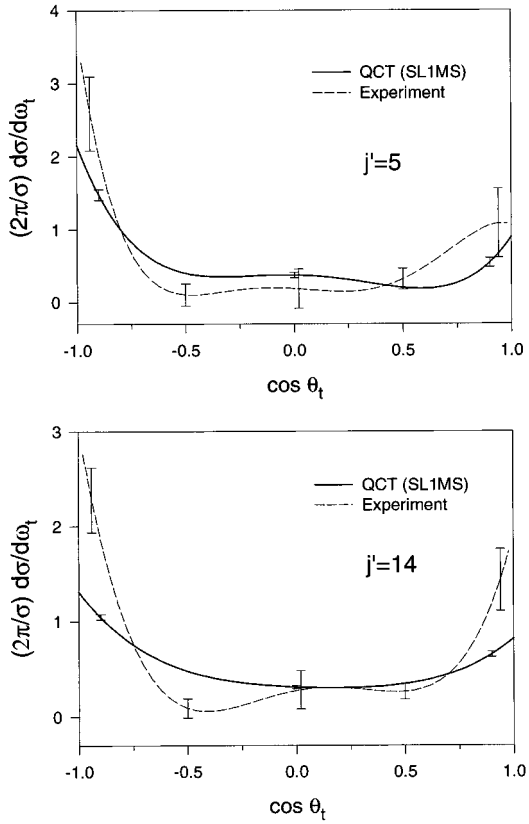

Figure 6. As in Figure 2, but comparing the experimental and QCT-derived DCSs. The solid lines are the QCT results, and the dashed lines are experimental best fits with errors. All errors shown represent one standard deviation.

are shown in Figures 9a,b and 10a. The rotational alignment of the Π(A′) $N' = 14$ state is marginally larger than that for the corresponding $N' = 5$ level, and the latter exceeds significantly the alignment of the A″ levels. Note that some of the PDDCSs for the $N' = 5$, A″ level are of opposite sign to those of the A′ level. Despite the poor signal−to−noise apparent in some some of the composite profiles, it was found that the general structures of the returned PDDCSs were quite robust. The value of $\bar{\beta}$ employed was found to be quite important; use of a velocity−dependent $\beta(O(^1D_2))$ tending to low values at low precursor velocities was found to significantly improve the fits, particularly to the $D_0^2(0,2;v_p)$ and $D_0^2(2,2;v_p)$ profiles. However, the polarization parameters returned by such an analysis are little changed from those in Table 1.

The QCT calculated PDDCSs 20, 21−, and 22+ are shown in Figures 9c and 10b for the two reactive channels $j' = 5$ and $j' = 14$. The results for the PDDCS 20 indicate strong alignment for extreme backward and forward scattering, which corresponds to the limit of $\mathbf{j}'$ perpendicular to $\mathbf{k}$ as required by angular momentum conservation in the limit of ($j = 0$) in H_2. The PDDCS 20 becomes nearly isotropic, however, for sideways scattering. Inspection of the PDDCS 22+, which is negative for all scattering angles, reveals an noticeable preference for an alignment of $\mathbf{j}'$ along the y axis as opposed to the x axis. Compared with the QCT calculated PDDCSs, the experimentally derived PDDCSs are generally larger, a feature also evident from the polarization parameters, a_q^k, presented below. However, the shapes (and signs) of the theoretical PDDCSs compare very favorably with the experimentally extracted ones for the Π(A′) lambda-doublet levels. As noted above, the polarization of the $N' = 5$, Π(A″) level is very different to that for Π(A′) and is inconsistent with the QCT predictions, which do not distinguish lambda-doublet component.

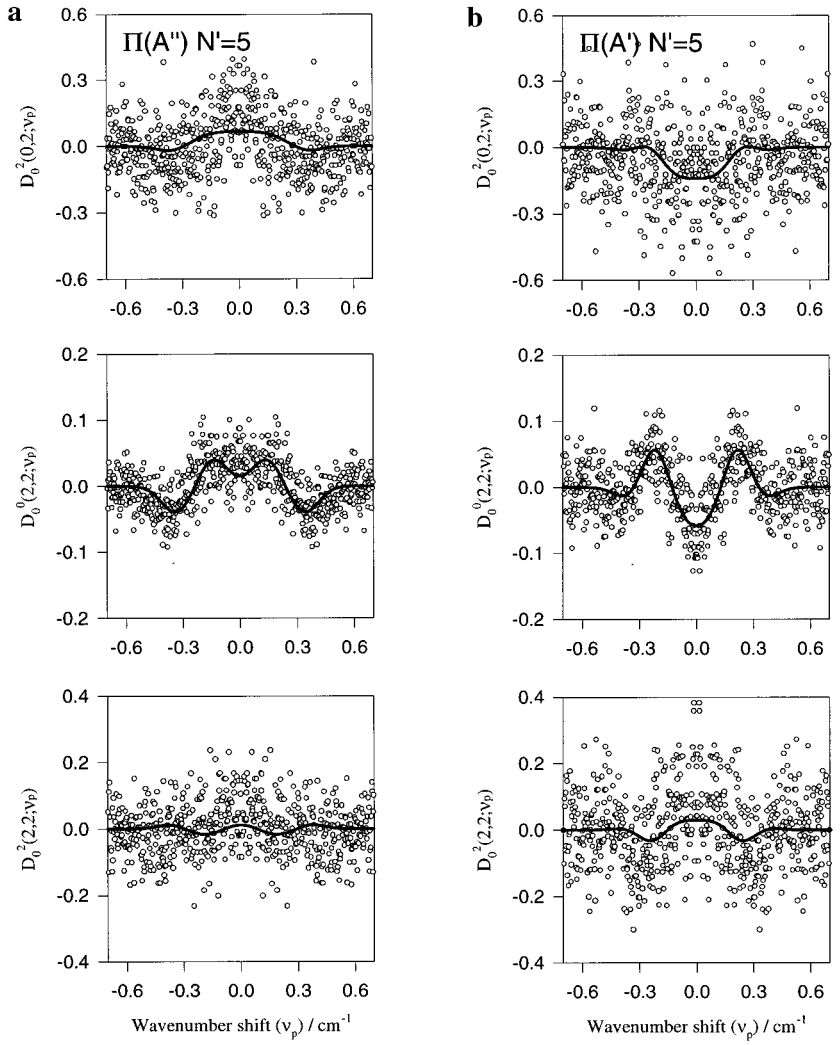

Figure 7. As in Figure 1, but showing experimental composite profiles $D_0^2(0,2,v_p)$ (top panels), $D_0^0(2,2;v_p)$ (middle panels), and $D_0^2(2,2;v_p)$ (lower panels) for (a) OH(v'=0,N'=5,A″), and (b) OH(v'=0,N'=5,A′). The experimental data, which reflect the laboratory rotational angular momentum polarization of the OH products, are shown as points, and the solid lines are the fits to the data. The derived PDDCSs are shown in Figure 9a,b.

One convenient way of visualizing the angular momentum polarization is in the form of a polar plot, displaying the probability of finding the angular momentum vector at angles θ_r, ϕ_r with respect to the CM (*xz*) scattering plane. The reconstruction of the probability distribution from the present experimental data is necessarily incomplete, however, since the latter are restricted to the first two even *k* moments of the expansion in eq 3 (see further discussion in section IVC). Figure 11 displays the experimentally derived distributions for the Π-(A′) and Π(A″) levels, averaged over all scattering angles, which can be compared with those predicted via QCT calculation employing even moments with $k \leq 2$ only, shown in Figure 12. The alignment parameters, a_q^k for $k = 2$, upon which these plots are based are shown in Table 1. The new dynamical information contained in the plots is that concerning the dihedral angle distribution. Both the experimental data for the A′ levels and the QCT data display preferential alignment along the CM frame *y* axis (i.e., perpendicular to the scattering plane): for the A″ level the experimentally derived alignment is, in contrast, preferentially in the *xz* scattering plane. Note further that the angular momentum alignment within the CM *xz* scattering plane, again for both the QCT data and the A′ levels, is tilted slightly away from the CM *x* axis, a subtle feature which is also evident in the QCT calculated polar plots (and which is highlighted by the dark points in the figures). The origin of the latter behavior might be traced back to a preferential alignment of **j**′ perpendicular to **k**′: the QCT calculations, to be presented in full elsewhere,[27] suggest significantly greater polarization of **k**′⊥**j**′ compared with that evident in the **k**−**j**′ correlation. For reaction with rotationless reactant molecules, and in the limit of extreme backward scattering, corresponding to **k**′ lying along the −*z* axis, **j**′ must lie in the CM *xy* plane by angular momentum conservation. In reality, the *average* scattering angle for the $j' = 5$ and 14 fragments will be less than 180°, and on average both **k**′ and **j**′ will be tilted away from the −*z* and the +*x* directions, respectively, as observed.

IV. Discussion

Although the dynamics of the reaction under investigation,

$$O(^1D_2) + H_2(v=0) \rightarrow OH(^2\Pi_i; v'=0, N', f) + H$$

have been studied under bulb conditions at 300 K, the experiments have been conducted under near state-to-state conditions, since the population of H_2 in levels $v > 0$ is negligible, and because of the nuclear spin statistics, the rotational state population follows the ordering $[j = 1] > [j = 2] > [j = 0] \gg [j > 2]$. For the lower OH rovibrational states, the translational exoergicity is quite significant: 177 kJ mol^{-1} for OH(N'=5). In contrast, because of the low reduced mass, the experimental collision energies, E_t, are much smaller and lie in the range 12 ± 7 kJ mol^{-1}.

In principle, collisions between $O(^1D_2)$ and H_2 could access five different PESs, the lowest of which is deeply bound and

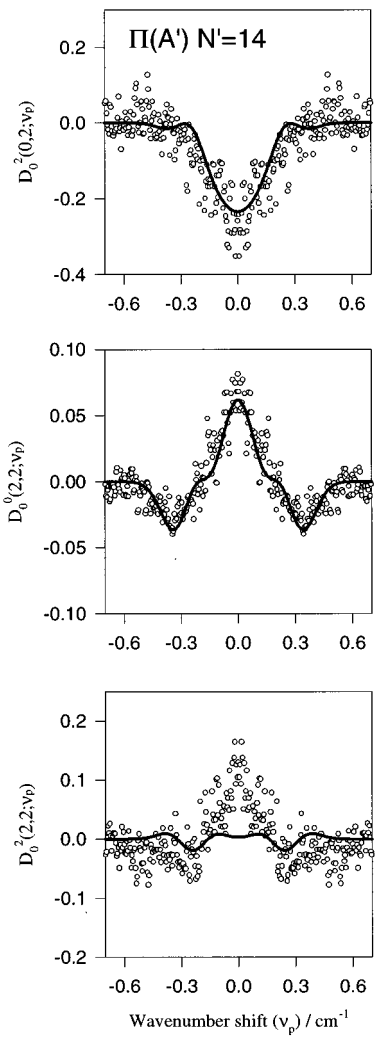

Figure 8. As in Figure 7, but for OH(v'=0,N'=14,A′). The derived PDDCSs are shown in Figure 10a.

highly anisotropic, correlating with the ground (^{1}A′) electronic state of H_2O. It is predicted to present little or no barrier to reaction.[22,28,29] In contrast, the excited PESs, which would correspond, in a linear configuration, to $^1\Pi$ and $^1\Delta$ states, are expected to display entrance barriers, with the $^1\Delta$ state being strongly repulsive.[28,29] The ground-state PES favors an insertion mechanism, leading to the highly excited rotational state distribution among the scattered OH fragments.[30] There is a marked propensity for preferential population of the Π(A′) lambda-doublet levels.[30]

A. State−Resolved Differential Cross Sections and Excitation Functions. Despite the very deep potential energy well, the absence of any significant exit barrier and the high exoergicity of the reaction should militate against long-lived reactive trajectories[31] or scattering resonances[32]—not withstanding the appearance of both forward and backward components in the total DCS.[12,33,34] Opinion has favored an insertion mechanism involving the intermediacy of collision complexes with average lifetimes, $\langle\tau_d\rangle$, which are short in comparison with their rotational periods, $\langle\tau_r\rangle$.[35] When the DCSs are determined at the product-state−resolved level, however, either experimentally[12] or computationally, via QCT calculations,[12,23] greater subtleties are suggested, since the cross sections are strongly dependent on the choice of quantum state. Paradoxically, a hint of this was first revealed in an experimental study of the total DCS of the isotopic reaction

$$O(^1D_2) + HD \rightarrow OH + D \qquad (13)$$

by Che and Liu.[34] Their data could only be interpreted by assuming the nonseparability of the DCS and the kinetic energy release; i.e., the DCSs were dependent on the internal energy in the OH.

The QCT calculations for reaction 13,[23] and also for the present reaction 1,[12] prompted in part by this result, indicated a strong sensitivity to both the vibrational and rotational state of the scattered OH. The angular distribution of fragments generated in ($v' = 0$) shifted from the backward to the forward hemisphere as j' increased. Fragments generated in ($v' = 4$, j') were scattered symmetrically into the forward and backward hemispheres. This behavior could be correlated with estimates of the ratio $\langle\tau_d\rangle/\langle\tau_r\rangle$, where $\langle\tau_d\rangle$ is the mean duration of the (state-to-state) reactive trajectory and $\langle\tau_r\rangle$ is the mean rotational period of the insertion complex (estimated from the most probable state-to-state reactive impact parameter).[12] While τ_r remained sensibly constant at $\tau_r \approx 100$ fs, the QCT calculations predicted mean collision lifetimes that increased with the vibrational quantum number, v, from $\tau_d \approx 30$ fs for OH(v'=0,j') to $\tau_d \approx 100$ fs for OH($v' = 4$,j')—a time scale comparable with the estimated rotational period and consistent with the predicted forward−backward symmetric scattering for OH(v'=4).[23] Unfortunately, *experimental* confirmation of the QCT prediction is not helped by the unfavorable kinematics and the low kinetic energy release for scattering into OH(v'=4). The belief in the reliability of the predictions is predicated on an assessment of the accuracy of the QCT calculations or, more significantly, of the Schinke−Lester (SL1) PES[22] upon which they are based.

Fortunately these *can* be assessed by reference to the experimental DCSs and the associated product-state-specific excitation functions determined for OH(v'=0,N') (see Figures 2−6), where the experimental and QCT results for $N' = 5$ and $N' = 14$ are compared. The strongly focused backward scattering for OH(v'=0,N'=5), the shift toward the forward hemisphere when N' is increased to 14, and even the steep drop in the excitation function with increasing collision energy, necessary for the coherent analysis of the full set of Doppler contours, are all reproduced quite well. Anticipating later discussion, belief in the reliability of the calculations is reinforced further by their success in reproducing the patterns of rotational angular momentum polarization (see sections IIIB and IVC) and, a fortiori, by comparisons with the *experimentally* determined DCSs of OH(v'=0,N') *and* OH(v'=4,N') scattered from the reaction of $O(^1D_2)$ with CH_4 (where the kinematics are now highly favorable[13,14]), see below.

Two interim conclusions can be drawn at this stage:

(1) the reaction of $O(^1D_2)$ with H_2 proceeds via the intermediacy of short-lived collision complexes, with average lifetimes, $\langle\tau_d\rangle$, which increase with increasing vibration in the scattered OH and lie in the range $\langle\tau_d\rangle \leq \langle\tau_r\rangle$, their mean rotational period; (2) the state-resolved DCSs and excitation functions can be reproduced by QCT calculations which assume the predominance of an insertion reaction on the ^{1}A′ ground state PES, with no entrance barrier.

B. Comparisons with the Reaction of $O(^1D_2)$ with CH_4. Figure 13 shows the Schinke−Lester SL1 PES for the $O(^1D_2)$/H_2 system, plotted the same way as the corresponding ground-state ab initio PES for $O(^1D_2)/CH_4$, shown in Figure 5 of ref 36. The similarity of the two surfaces is very striking. Each presents a deep well, centered at the equilibrium geometry of H_2O or CH_3OH; the detailed contours of the two surfaces around the central well are remarkably alike, including the "humps" in the entrance and exit regions of each PES, which reflect the

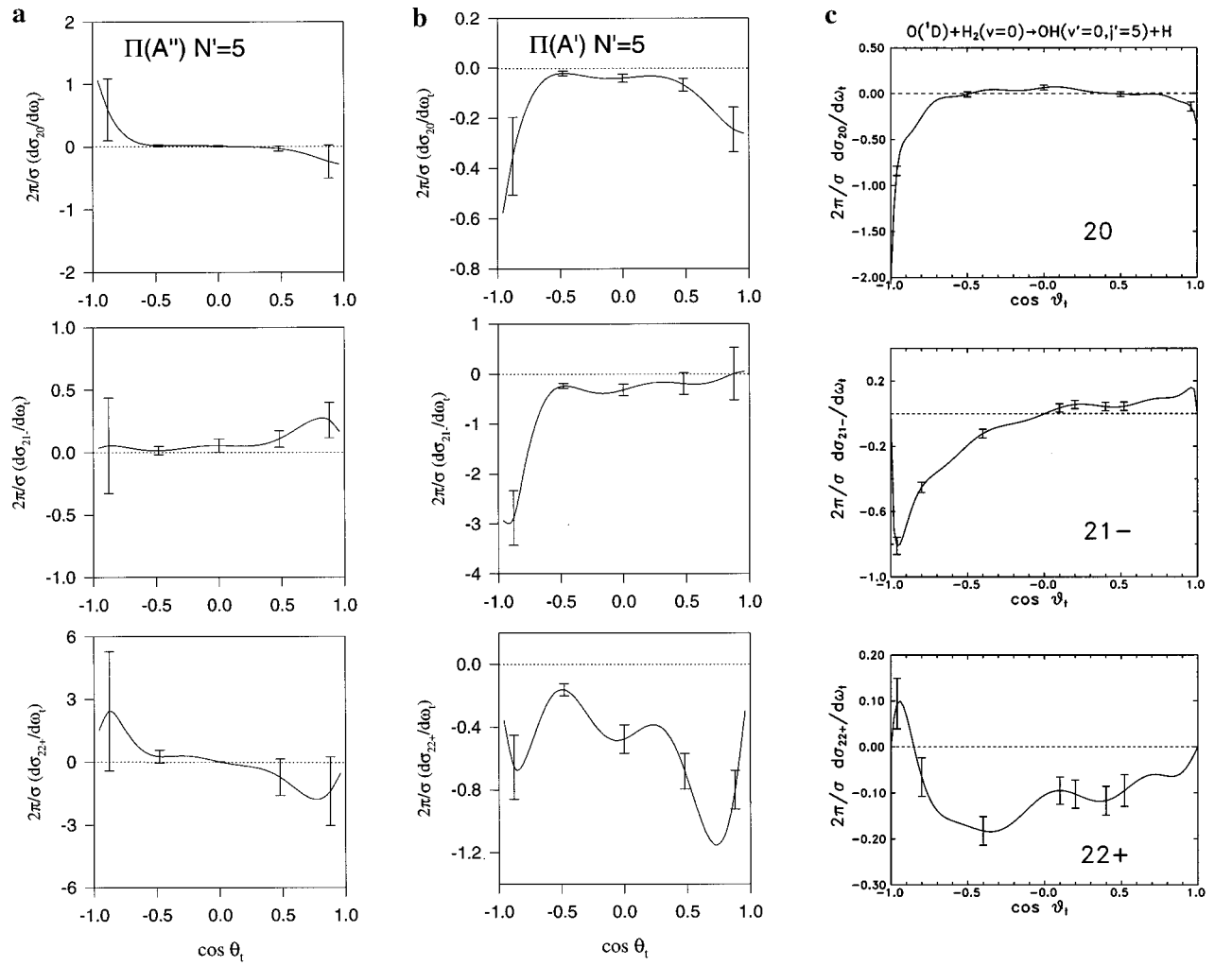

Figure 9. Three PDDCSs, $(2\pi/\sigma)(d\sigma_{20}/d\omega_t)$ (top panels), $(2\pi/\sigma)(d\sigma_{21-}/d\omega_t)$ (middle panels), and $(2\pi/\sigma)(d\sigma_{22+}/d\omega_t)$ (bottom panels) derived from the data shown in Figure 7 for (a) OH(v'=0,N'=5,A″) and (b) OH(v'=0,N'=5,A′). The error bars represent two standard deviations. QCT-derived PDDCSs for OH(v'=0,j'=5) are shown in (c). The error bars represent one standard deviation, and the calculations were performed at a fixed collision energy of 0.1 eV.

conical intersections between the linear $^1\Sigma^+$ and $^1\Pi$ electronic states. Of course, the dynamics of the reaction

$$O(^1D_2) + CH_4 \rightarrow OH + CH_3 \qquad (14)$$

will be influenced by the polyatomic nature of the target molecule, but the similarities in the two PESs suggest the retention of some dynamical features in common with those for the reaction with H_2.

Experimental polar scattering maps for OH(v'=0,N'=5) and OH(v'=4,N'=8), generated from the reaction of $O(^1D_2)$ with CH_4,[14] are shown in Figure 14. They may be compared with the corresponding maps generated from the $O(^1D_2)/H_2$ QCT results for OH(v'=0,j'=1−10) and OH(v'=4,j'=1−17) (Figure 15). The similarities are extraordinary. The two scattering maps for OH(v'=0) each display a sharp backward peak and a weak forward peak; those for OH(v'=4) approach forward−backward symmetry. The **k**,**k**′ vector correlations are almost identical. The scalar distributions in the strongly exoergic channels leading to OH(v'=0) are very different, however, since the kinetic energy released in the product-state-resolved, polyatomic reaction

$$O(^1D_2) + CH_4 \rightarrow OH(2\Pi_i;v'=0,N'=5) + CH_3 \qquad (15)$$

is low. Most of the exoergicity appears as internal excitation in the unobserved, polyatomic CH_3 fragment, implying considerable vibrational redistribution (IVR) within an (OCH_4) collision complex.[14] Indeed, the state-resolved DCSs were interpreted in terms of different state-resolved opacity functions for OH(v'=0) and OH(v'=4), with the former peaked at low impact parameters and leading to collision complexes with rotational periods in the range $\langle\tau_r\rangle \leq 2$ ps.[14] They can be compared with the "real-time" determination of a collision complex lifetime $\langle\tau_d\rangle \simeq 3$ ps, based upon the rate of appearance of OH(v'=0,N') following the photodissociation of a van der Waals complex of O_3 and CH_4.[37]

The QCT "clock", employed in analyzing the dynamics of the reaction with H_2, leads to collision complex lifetimes and rotational periods lying within the range 30−100 fs. The real time and "rotational clocks" used to analyze the results for CH_4 led to time scales typically an order of magnitude longer in duration[14]—time enough for extensive (if not complete) IVR—associated, no doubt, with the increased moment of inertia and the polyatomic character of the collision complex. However, the remarkable similarity between the two sets of scattering maps, shown in Figures 14 and 15 for OH(v'=0) and OH(v'=4), suggests the *relative* time scales, $\langle\tau_d\rangle/\langle\tau_r\rangle$, in the two channels are little changed when CH_4 is substituted for H_2. When OH is scattered into the highest vibrational levels ($v \geq 4$), $\langle\tau_d\rangle \sim \langle\tau_r\rangle$, and the DCS displays strong forward and backward peaks. When OH is generated in the lowest quantum states ($v' = 0$, $N'(j') \simeq 0$), $\langle\tau_d\rangle < \langle\tau_r\rangle$, and the fragments are scattered predominantly into the backward hemisphere, implying perhaps, the predominance of low impact parameters[12,14] and transition-

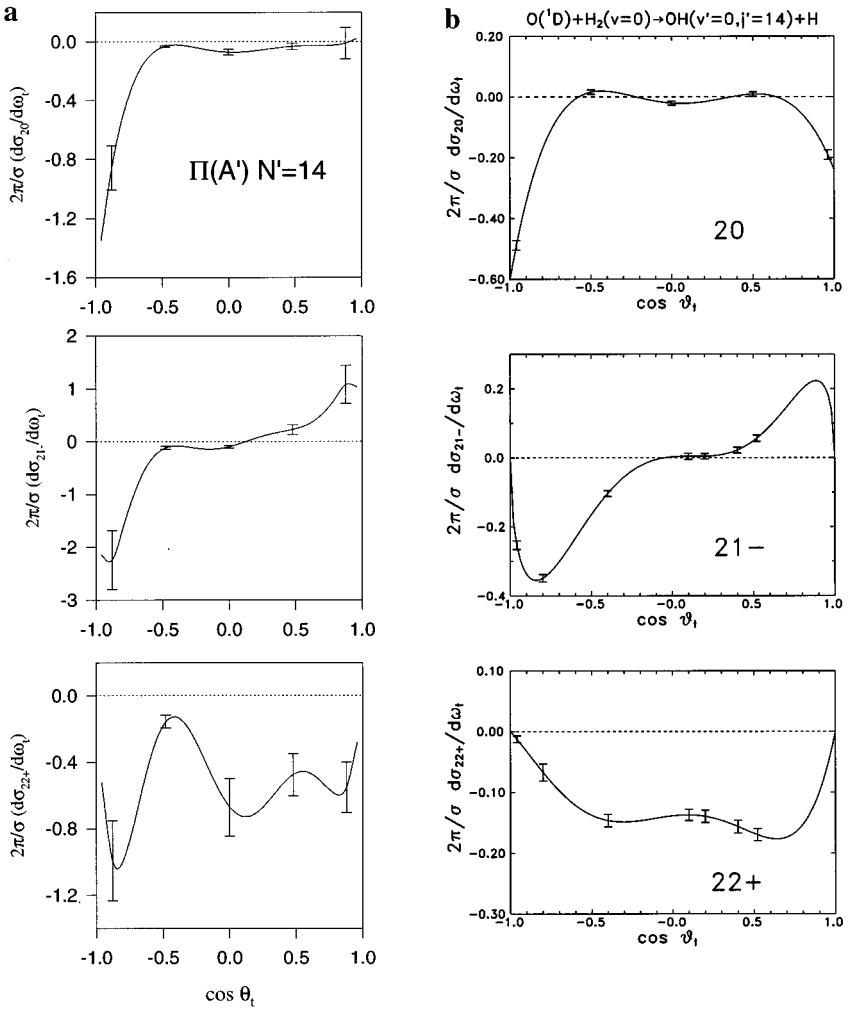

Figure 10. As in Figure 9; the three experimentally derived PDDCSs for OH(v'=0,N'=14,A′) are shown in (a). The QCT-derived PDDCSs for OH(v'=0,j'=14) are shown in (b).

TABLE 1: State-Resolved, QCT Calculated and Experimentally Determined, Polarization Parameters with $k = 2$ for the OH Products of the Reaction of O($^1D_2$) with H_2[a]

OH state	a_0^2	a_{1-}^2	a_{2+}^2
Π(A′); $v' = 0$, $N = 5$	-0.23 ± 0.05	-1.11 ± 0.23	-1.05 ± 0.21
Π(A″); $v' = 0$, $N = 5$	$+0.11 \pm 0.25$	-0.18 ± 0.21	-0.03 ± 1.85
Π(A′); $v' = 0$, $N = 14$	-0.32 ± 0.10	-0.30 ± 0.31	-1.05 ± 0.27
$v' = 0$, $N = 5$ QCT	-0.140 ± 0.005	-0.198 ± 0.006	-0.207 ± 0.009
$v' = 0$, $N = 14$ QCT	-0.120 ± 0.003	-0.086 ± 0.003	-0.260 ± 0.006

[a] The polarization parameters are obtained by averaging the PDDCSs over all CM scattering angles and are defined in refs 7 and 8. The experimental data are specific to each lambda doublet level: the QCT data, of course, do not distinguish lambda-doublet components. The uncertainties in the experimental data represent two standard deviations (2σ), whereas the QCT error bounds are single standard deviations (1σ).

state structures of the form O—H—H (or O—H—CH_3) accessed by rotation of the target molecule under the influence of the strong anisotropic interaction potential. The latter hypothesis concerning the O(^{1}D) + H_2 reaction will be explored in more detail elsewhere.[27]

C. Rotational Polarization. The state−resolved rotational polarizations of the OH products provide additional insight into the role of collision complexes and the mechanism of their formation and decay. Herschbach and co-workers[38] have presented angular distributions, $P(\theta_t)$, $P(\theta_r)$, and $P(\phi_r)$ in the present notation, for triatomic A + BC(j=0) reactions proceeding via "separable" statistical complexes in the kinematic limits $\mathbf{l} \rightarrow \mathbf{j}'$ and $\mathbf{l} \rightarrow \mathbf{l}'$. A common feature of these distributions is the symmetry they possess about $\pi/2$ (for $P(\theta_t)$ and $P(\theta_r)$) or π (for $P(\phi_r)$): the first of these symmetries corresponds to the familiar forward−backward symmetry in the DCS expected in the limit of a long-lived complex. Of particular note are the predicted forms of the dihedral angular distributions, $P(\phi_r)$, which are either isotropic ($\mathbf{l} \rightarrow \mathbf{l}'$) or strongly peaked at $\phi_r = 0$ and π ($\mathbf{l} \rightarrow \mathbf{j}'$). In the present *state-resolved* measurements, neither kinematic limit is appropriate, since the reactant orbital angular momentum is shared between that of the products and the OH rotational angular momentum, although the channel leading to OH(N'=5) comes closest to approaching the $\mathbf{l} \rightarrow \mathbf{l}'$ limit. Note, however, that neither the QCT nor the experimentally derived $k = 0$, 2 dihedral angular distributions for OH $N' = 5$ and 14, which show maxima probabilities at $\phi_r = \pi/2$ and $3\pi/2$, approach those expected for a statistical complex, in accord with expectation based on analysis of the DCSs alone.

Although the rotational polarization data contain valuable information about angular momentum disposal in the reaction, they should be interpreted with caution since, as noted in section IIIB, only moments with $k = 0$, 2 have thus far been determined. A recent QCT study of the direct F + H_2 reaction[10] has demonstrated that (low-order) odd moments of the angular momentum distribution can be very significant, and the resulting

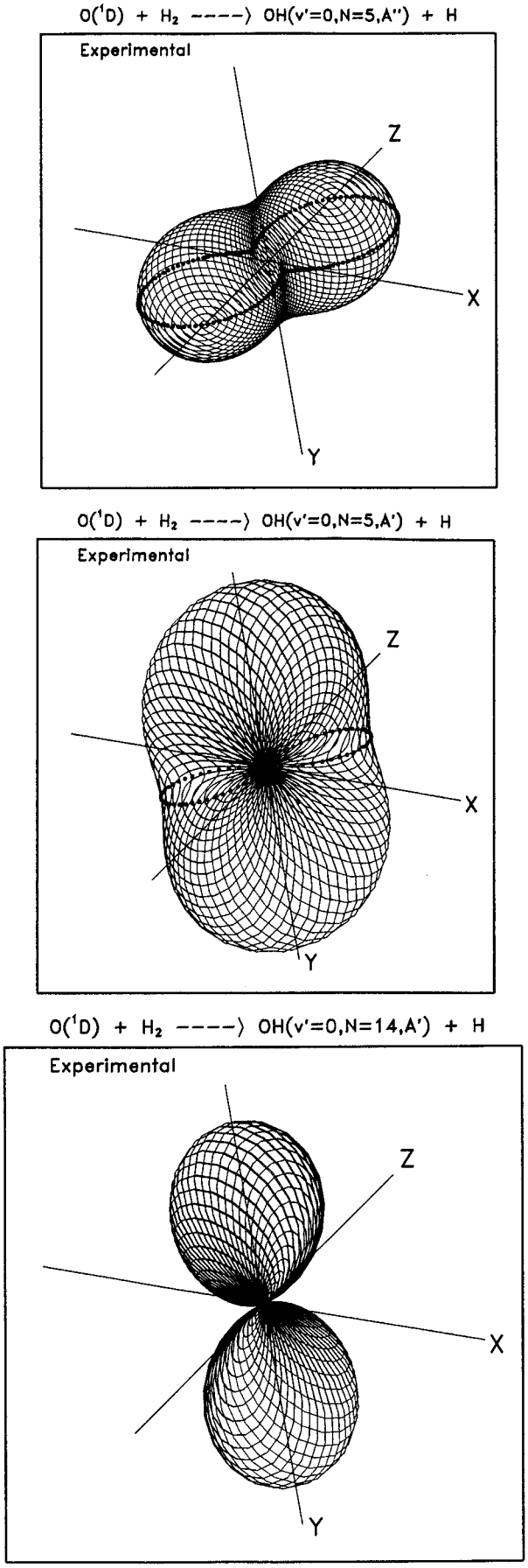

Figure 11. Experimentally derived polar plots of the (scattering angle θ_t averaged) rotational polarization, $P(\theta_r,\phi_r)$, including only even moments with $k \leq 2$ for OH(v'=0,N'=5,A'') (top), OH(v'=0,N'=5,A') (middle) and OH(v'=0,N'=14,A') (bottom). For clarity, the angular momentum distribution in the *xz* plane has been highlighted by dark points.

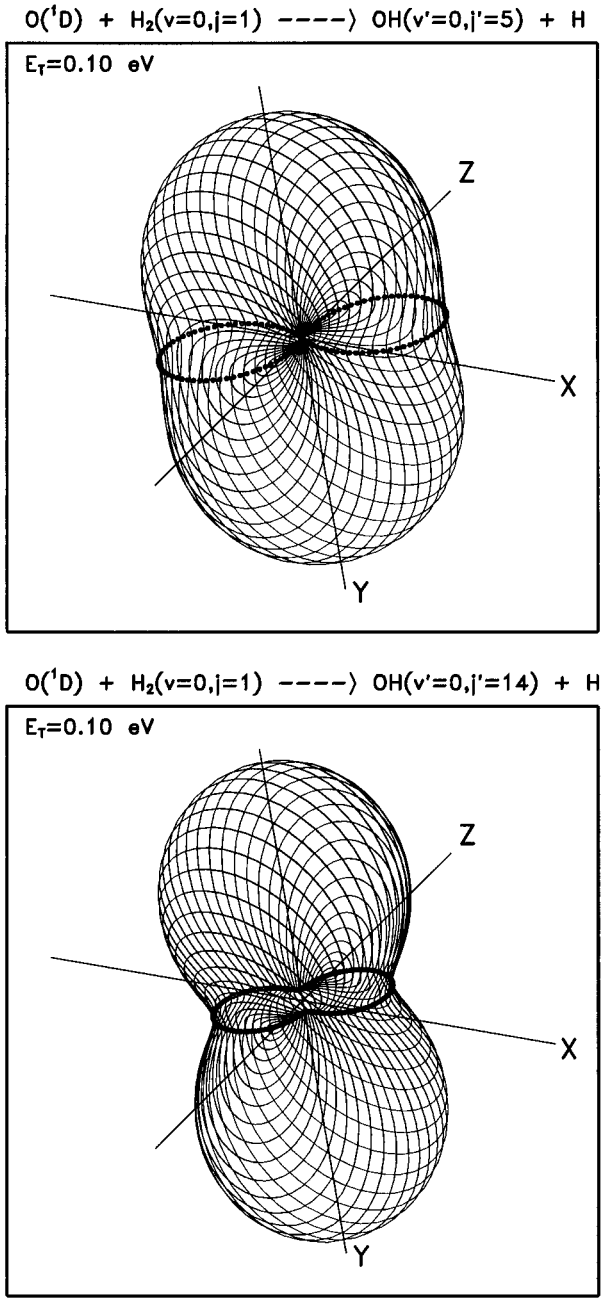

Figure 12. As in Figure 11, but showing the QCT-derived, scattering angle averaged, polar plot of the product rotational angular momentum distribution: upper panel, OH(v'=0,j'=5); lower panel, OH(v'=0,j'=14). The calculations were made at a fixed collision energy of 0.1 eV, and only even moments with $k \leq 2$ have been included in these plots.

orientation along the CM *y* axis can be a key indicator of the reaction stereodynamics. While the comparison between experimental (Figure 11) and QCT (Figure 12) derived polarization for moments with $k = 0$, 2 is satisfactory, and indeed lends further credence to the potential energy surface employed in the QCT calculations, to what extent do the polar plots shown in Figures 11 and 12 reflect the full angular momentum distribution? Figure 16 shows QCT calculated polar plots for the $j' = 5$ and 14 levels analogous to those shown in Figures 11 and 12, this time including even and odd moments of the distribution with $k \leq 10$. (The polar plots are little altered if they are generated with moments $k \leq 15$.) Clearly, the full angular momentum polarization distribution displays more detailed structure than can be obtained from inclusion of low-order even moments alone—more significantly, however, the distributions reveal substantial variations in angular momentum

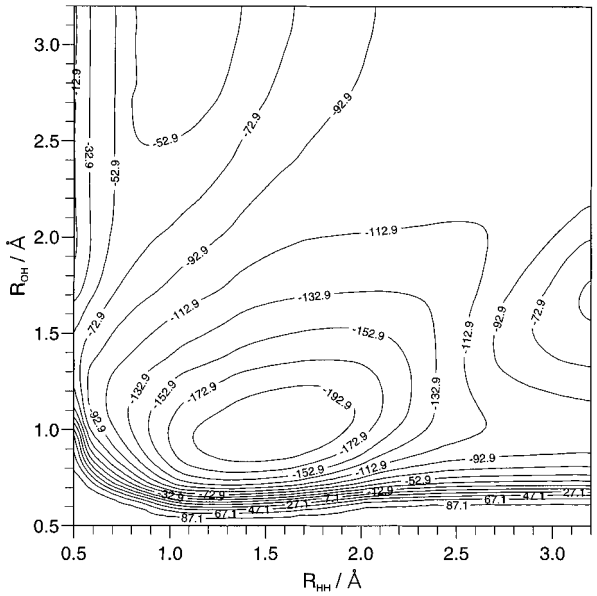

Figure 13. Contour plot of the ground-state Schinke−Lester (SL1MS) potential energy surface for the reaction O($^1D_2$) + H_2 as a function of the OH and HH bond lengths, the remaining OH bond length being optimized to minimize the energy. The contours are labeled in kcal mol^{-1}, separated in 20 kcal mol^{-1} increments, and the axes are scaled in angstrom units. This figure should be compared with Figure 5 of ref 36, which shows an analogous plot for the O($^1D_2$) + CH_4 reaction.

disposal with quantum state, and net orientation along the CM *y* axis, albeit of lower magnitude than the near limiting orientations observed for the F + H_2 reaction.[10] As will be described in detail elsewhere,[27] the full distributions provide unequivocal evidence for the role of transitory *insertion* complexes, at least in the QCT calculations on the SL1 PES.

V. Conclusions and Look Forward

The new results demonstrate very forcibly the importance of detailed, state-resolved experiments, coupled with high-quality scattering computations, in probing and interpreting the dynamics of atomic and molecular reactions. The product-state-resolved differential cross sections for the insertion reaction of O($^1D_2$) with H_2 (or CH_4) are highly sensitive to the products' quantum state; the near symmetry of the state-averaged differential cross section for the reaction of O($^1D_2$) with H_2[33] belies its underlying complexity. The remarkable success of quasiclassical trajectory calculations, conducted on the Schinke−Lester PES, in predicting this complexity and a fortiori in providing quantitative agreement with the product-state-resolved linear and angular momentum distributions and their state-resolved excitation functions, has been of signal importance in aiding their dynamical interpretation. The overriding importance of both absolute and relative time scales, the relative duration of the collision complexes and their rotational periods, has been quantified, together with their role in determining the vectorial linear, $P(\mathbf{k},\mathbf{k}')$, and angular momentum, $P(\mathbf{k},\mathbf{k}',\mathbf{j}')$, distributions.

The success of the trajectory calculations, which assumed reaction over the ground-state ($^1A'$) potential energy surface, implicates the reaction of O($^1D_2$) atoms with $M_j = 0$ (in the molecular frame), i.e., the component oriented with its empty

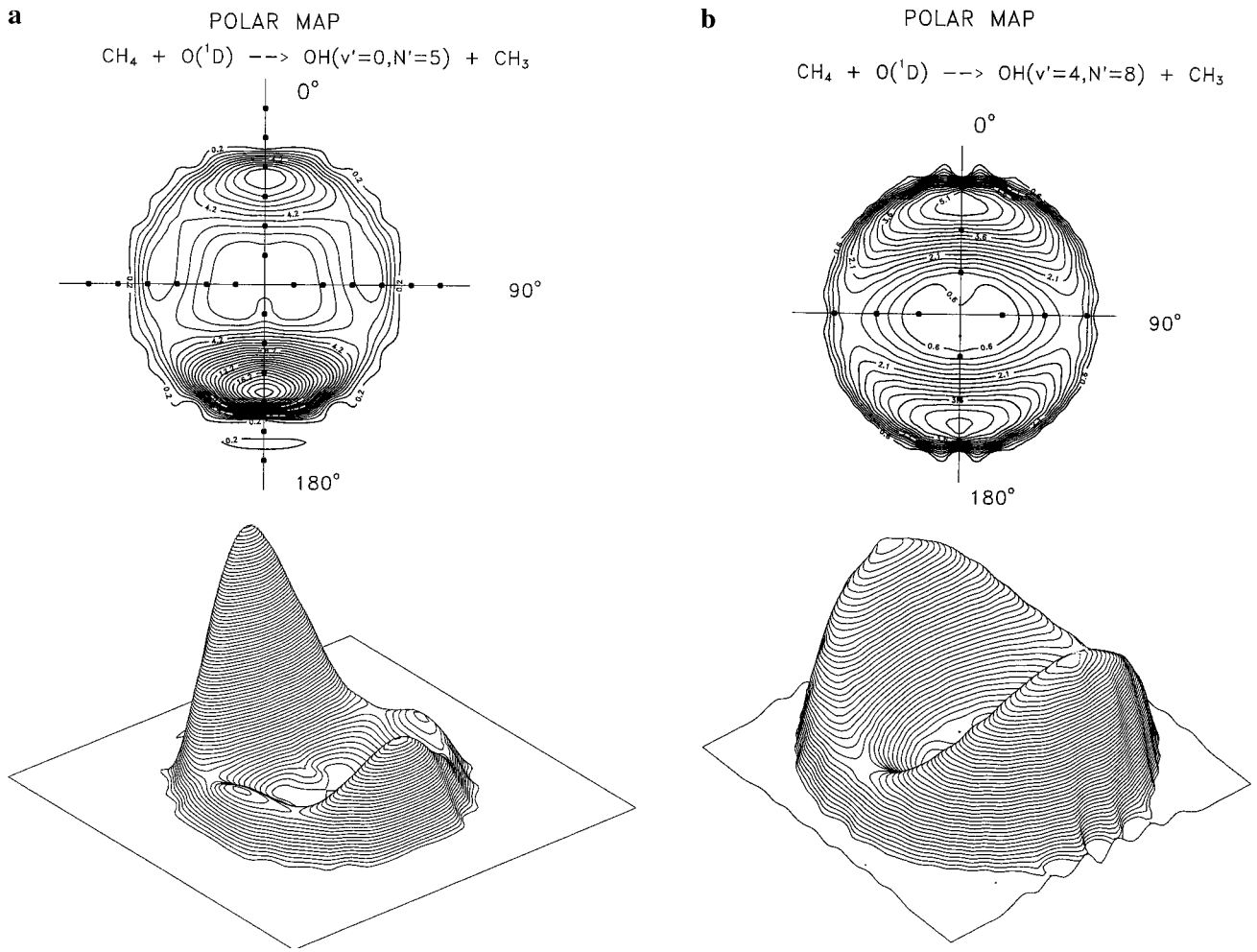

Figure 14. Experimentally derived, velocity-scattering angle, state-resolved polar maps for the reaction O($^1D_2$) + CH_4:[13,14] (a) OH(v'=0,N'=5) and (b) OH(v'=4,N'=8). Forward scattering (0°) corresponds to the direction of the scattered OH with respect to the direction of the incoming atom.

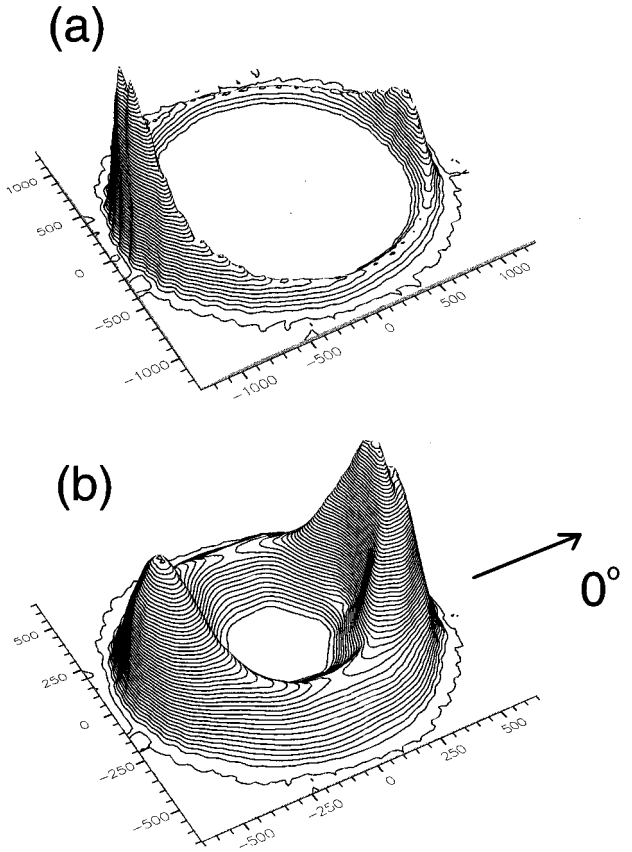

Figure 15. QCT-calculated, velocity−scattering angle, state-resolved polar maps for the $O(^1D_2) + H_2$ reaction: (a) OH(v'=0,j'=0−10) and (b) OH(v'=4,j'=0−17). Both maps were generated at a fixed collision energy of 0.1 eV. The direction of forward scattering is defined the same as in Figure 14, and the scale is in m s^{-1}.

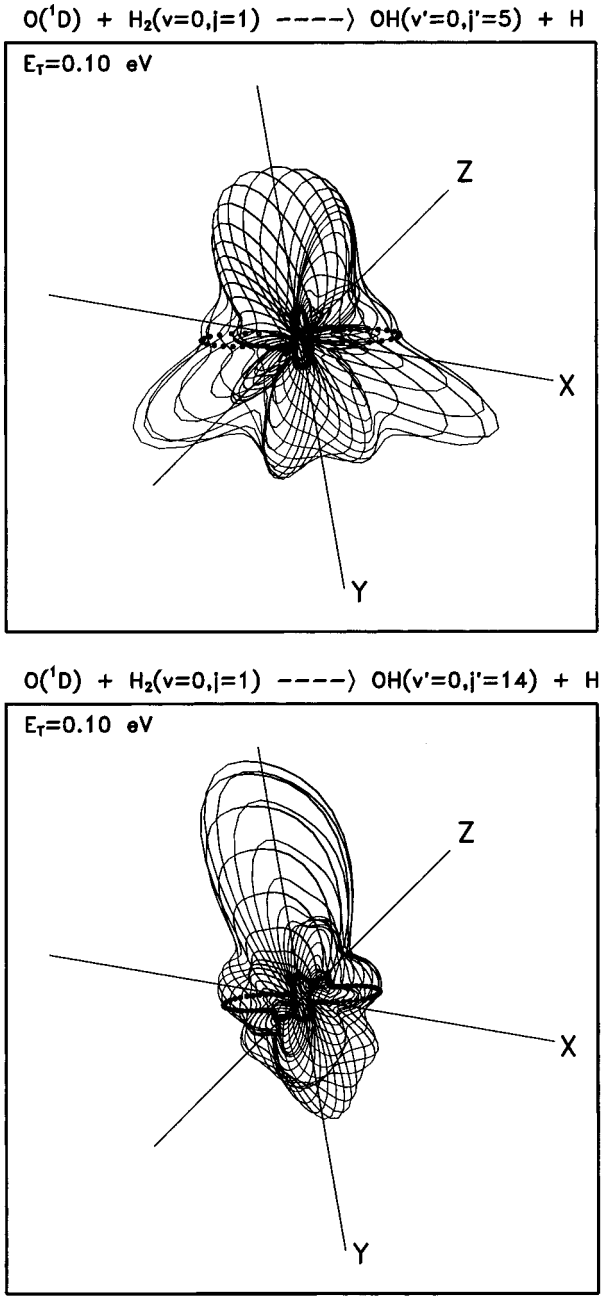

Figure 16. As in Figure 12, but showing the QCT polar plot of the OH angular momentum polarization distribution for *all* moments with $k \leq 10$: $v' = 0$, $j' = 5$ (upper panel) and $v' = 0$, $j' = 14$ (lower panel).

p-orbital lobe directed toward the molecular reagent to access directly the highly attractive $^1A'$ PES. Insertion dynamics on the $^1A'$ surface are also consistent with the preferential population of the $\Pi(A')$ lambda-doublet component of OH; the reaction dynamics do not appear to be influenced by the photolytic production of orbitally aligned atoms[18,19] with $M_j \neq 0$ (referenced to their recoil velocity). This could be ascribed either to their reorientation during collision or to their inelastic scattering from excited $^1\Pi$ or $^1\Delta$ surfaces. The much reduced rotational angular momentum polarization in OH fragments generated from H_2, in the $\Pi(A'')$ lambda-doublet state, parallels the behavior found earlier for the reaction of $O(^1D_2)$ with CH_4[13] and of H with O_2.[39] The similarities further reinforce the proposed population of OH($\Pi(A'')$) through nonadiabatic transitions in the asymptotic regions of the exit channel, a proposal originally made by Hall and co-workers to explain the analysis of the polarization data in the H/O_2 system.[39]

What of the future? Measurements of rotational angular momentum orientation should be possible using circularly polarized probe laser radiation to affirm (or not!) the QCT predictions and thereby gain insight into the otherwise unobserved correlations between $\mathbf{j}'$ and the reagent and product orbital angular momenta, $\mathbf{l}$ and $\mathbf{l}'$. As the lifetimes of the collision complexes approach the average duration of their rotational periods, the dihedral angular distribution of the products' rotational angular momentum, $\mathbf{j}'$, should become symmetric about the angle, $\phi_r = \pi$, in much the same way as the differential cross sections become symmetric about the scattering angle, $\theta_t = \pi/2$.[27,38] With H_2 as the molecular reagent, kinematic constraints hamper prevent dynamical measurements when the kinetic energy release is low. These problems can be reduced, however, either by substituting the heavier D_2 molecule for H_2 and/or by coexpanding the reagents in a molecular beam to reduce the thermal spread of collision velocities. Further experimental studies of HD[34] should also be rewarding; a QCT study of the channel leading to OH(v'=0,N'=0−10) has predicted a propensity for forward scattering,[23] the exact opposite of the angular distribution from H_2. Finally, accurate measurements of the speed dependence of the translational anisotropy, $\beta(O(^1D_2))$ from N_2O, at low speeds would aid further the quantitative analysis of the polarization data.

Acknowledgment. We are grateful to the EPSRC for a research grant and the award of studentships to A.J.A. and J.S. and to the Spanish−British exchange program "Acciones Integradas". F.J.A. and L.B. gratefully acknowledge the financial support by the DGICYT of the Ministry of Education and

Culture of Spain under Grant PB95−0918−C03. We also thank Prof. Itamar Burak (Tel Aviv University) and Dr. Yo Fujimura (Kyoto University), who were involved in some of the early experimental work, Monbuso for funding YF's exchange visit, and the EPSRC for a Visiting Fellowship for I.B.

References and Notes

(1) Brouard, M.; Simons, J. P. In *Chemical Dynamics and Kinetics of Small Free Radicals*; Wagner, A., Liu, K., Eds.; World Scientific: Singapore, 1995; p 795.

(2) (a) Orr-Ewing, A. J.; Zare, R. N. *Annu. Rev. Phys. Chem.* **1994**, *45*, 315. (b) Orr-Ewing, A. J.; Zare, R. N. In *Chemical Dynamics and Kinetics of Small Free Radicals*; Wagner, A., Liu, K., Eds.; World Scientific: Singapore, 1995; p 936. (c) Orr-Ewing, A. J. *J. Chem. Soc., Faraday Trans.* **1996**, *92*, 881.

(3) (a) Brouard, M.; Duxon, S.; Simons, J. P. *J. Chem. Phys.* **1992**, *97*, 7414. (b) Brouard, M.; Duxon, S.; Enriquez, P. A.; Simons, J. P. *J. Chem. Soc., Faraday Trans.* **1993**, *89*, 1432.

(4) (a) Simpson, W. R.; Orr-Ewing, A. J.; Zare, R. N. *Chem. Phys. Lett.* **1993**, *212*, 163. (b) Simpson, W. R.; Orr-Ewing, A. J.; Kandel, S. A.; Rakitzis, T. P.; Zare, R. N. *J Chem. Phys.* **1995**, *103*, 7299, 7313.

(5) Aoiz, F. J.; Brouard, M.; Enriquez, P. A.; Sayos, R. *J. Chem. Soc., Faraday Trans.* **1993**, *89*, 1427.

(6) Shafer, N. E.; Orr-Ewing, A. J.; Simpson, W. R.; Xu, H.; Zare, R. N. *Chem. Phys. Lett.* **1993**, *212*, 155.

(7) Shafer, N. E.; Orr-Ewing, A. J.; Zare, R. N. *J. Phys. Chem.* **1995**, *99*, 7591.

(8) Aoiz, F. J.; Brouard, M.; Enriquez, P. A. *J. Chem. Phys.* **1996**, *105*, 4964.

(9) (a) Case, D. E.; Herschbach, D. R. *Mol. Phys.* **1975**, *30*, 1537. (b) Barnwell, J. D.; Loeser, J. G.; Herschbach, D. R. *J. Phys. Chem.* **1983**, *87*, 2781.

(10) Aoiz, F. J.; Brouard, M.; Herrero, V. J.; Sáez Rabános, V.; Stark, K. *Chem. Phys. Lett.* **1997**, *264*, 487.

(11) Miranda, M. P.; Clary, D. C. Submitted to *J. Chem. Phys.*

(12) Alexander, A. J.; Aoiz, F. J.; Brouard, M.; Burak, I.; Fujimura, Y.; Short J.; Simons, J. P. *Chem. Phys. Lett.* **1996**, *262*, 589.

(13) Brouard, M.; Lambert, H. M.; Short J.; Simons, J. P. *J. Phys. Chem.* **1995**, *99*, 13571.

(14) Brouard, M.; Lambert, H. M.; Russell, C.; Short J.; Simons, J. P. *Faraday Discuss. Chem. Soc.* **1995**, *102*, 179.

(15) Dixon, R. N. *J. Chem. Phys.* **1986**, *85*, 1866.

(16) Docker, M. P. *Chem. Phys.* **1989**, *135*, 405.

(17) Brouard, M.; Lambert, H. M.; Rayner, S. P.; Simons, J. P. *Mol. Phys.* **1996**, *89*, 403.

(18) Suzuki, T.; Katayanagi, H.; Mo, Y.; Tonokura, K. *Chem. Phys. Lett.* **1996**, *256*, 90.

(19) Neyer, D. W.; Chandler, D.; Heck, A. Personal communication.

(20) Felder, P.; Haas, B.-M.; Huber, J. R. *Chem. Phys. Lett.* **1991**, *186*, 177.

(21) Aoiz, F. J.; Herrero, V. J.; Sáez Rábanos, V. *J. Chem. Phys.* **1992**, *97*, 7423 and references therein.

(22) Schinke, R.; Lester Jr., W. A. *J. Chem. Phys.* **1980**, *72*, 3754.

(23) Alexander, A. J.; Aoiz, F. J.; Brouard, M.; Simons, J. P. *Chem. Phys. Lett.* **1996**, *256*, 561.

(24) Aoiz, F. J.; Bañares, L.; D'ez--Rojo, T.; Herrero, V. J.; Sáez Rábanos, V. *J. Phys. Chem.* **1996**, *100*, 4071.

(25) Aoiz, F. J.; Bañares, L. *J. Phys. Chem.* **1996**, *100*, 18108.

(26) Aoiz, F. J.; et al. Manuscript in preparation.

(27) Alexander, A. J.; Aoiz, F. J.; Brouard M.; Herrero, V. J.; Simons, J. P. Manuscript in preparation.

(28) Walch, S. P.; Harding, L. B. *J. Chem. Phys.* **1988**, *88*, 7653.

(29) Ho, T.-S.; Hollebeek, T.; Rabitz, H.; Harding L. B.; Schatz, G. C. *J. Chem. Phys.* **1996**, *105*, 10472.

(30) Cleveland, C. B.; Jurisch, G. M.; Trolier, M.; Wiesenfeld, J. R. *J. Chem. Phys.* **1986**, *86*, 3253.

(31) Fitzcharles, M. S.; Schatz, G. C. *J. Phys. Chem.* **1986**, *90*, 3634.

(32) Peng, T.; Zhang, D. H.; Zhang, J. Z. H.; Schinke, R. *Chem. Phys. Lett.* **1996**, *248*, 37.

(33) Buss, R. J.; Casavecchia, P.; Hirooka, T.; Sibener, S. J.; Lee, Y. T. *Chem. Phys. Lett.* **1981**, *82*, 386.

(34) Che, D.-C.; Liu, K. *J. Chem. Phys.* **1995**, *103*, 5164.

(35) Koppe, S.; Laurent, T.; Naik, P. D.; Volpp, H.-R.; Wolfrum, J.; Arusi-Parpar, T.; Bar, I.; Rosenwaks, S. *Chem. Phys. Lett.* **1993**, *214*, 546 and references therein.

(36) Arai, H.; Kato, S.; Koda, S. *J. Phys. Chem.* **1994**, *98*, 12.

(37) van Zee, R. D.; Stevenson, J. C. *J. Chem. Phys.* **1995**, *102*, 6946.

(38) Kim, S. K.; Herschbach, D. R. *Faraday Discuss. Chem. Soc.* **1987**, *84*, 159.

(39) Kim, H. L.; Wickramaaratchi, M. A.; Zheng, X.; Hall, G. E. *J. Chem. Phys.* **1994**, *101*, 2033.